frontiers | Frontiers in Earth Science

TYPE Original Research
PUBLISHED 01 December 2025
DOI 10.3389/feart.2025.1731804

OPEN ACCESS

EDITED BY
Xiangguo Kong,
Xi'an University of Science and Technology, China

REVIEWED BY
Zhibo Zhang,
University of Science and Technology Beijing, China
Biao Kong,
Shandong University of Science and Technology, China

*CORRESPONDENCE
Yuqi Zhang,
zhangyuqi@cumt.edu.cn
Meiling Zhou,
zhoumeiling0303@163.com

RECEIVED 24 October 2025
REVISED 07 November 2025
ACCEPTED 19 November 2025
PUBLISHED 01 December 2025

CITATION
Yan Y, Zhang Y and Zhou M (2025) Investigation of the evolution of deformation field and crack propagation characteristics of sandstone containing an arched roadway. *Front. Earth Sci.* 13:1731804. doi: 10.3389/feart.2025.1731804

Investigation of the evolution of deformation field and crack propagation characteristics of sandstone containing an arched roadway

Yao Yan[1], Yuqi Zhang[2]* and Meiling Zhou[3]*

[1]Henan Pingmei Shenma Liangbei No.2 Mine Industry Co., Ltd., Xuchang, China, [2]School of Safety Engineering, China University of Mining and Technology, Xuzhou, China, [3]Huaneng Xindian Power Generation Co., Ltd., Zibo, China

In mining, tunneling, and other engineering activities, the stability and strength of the surrounding rock system are primarily governed by the dynamic evolution of crack initiation, propagation, and interconnection in the rock material. To investigate the fracture process of sandstone containing an arched roadway under uniaxial compression, yellow sandstone samples with arched roadways were prepared, and their displacement field, strain field evolution, and crack propagation characteristics were revealed using digital image correlation (DIC) technology. The results show that under uniaxial loading, the deformation and failure process of yellow sandstone samples containing arched roadways can be divided into four stages: initial compaction, elastic deformation, plastic deformation, and instability failure, with the peak stress measured at approximately 16 MPa. As the load increases, the displacement and strain fields evolve, and their values gradually increase. Before the load level reaches 70%, the displacement and strain values increase slightly, reaching approximately 0.3 mm and 0.01, respectively. During the accelerated crack growth stage, the displacement and strain values increase rapidly. At 100% load, the maximum displacement and strain values reach 0.4 mm and 0.03, respectively. After brittle failure, the instantaneous displacement and strain can increase to 1 mm and 0.06, respectively. During the loading process, the maximum principal strain of each crack around the arched roadway increases and evolves asynchronously. The strain distribution on the left and right sides of the roadway is significantly greater than that on the upper and lower sides, exhibiting a degree of symmetry. By analyzing the included angle of crack initiation and the horizontal and vertical displacement values at two points on either side of the crack initiation position, the relative displacement in the tangential and normal directions of each crack can be determined. Combined with difference calculations, the tensile and shear properties of the crack, along with the corresponding initiation time and stress, can be quantified. Under uniaxial loading, the cracks in the yellow sandstone samples with arched roadways are predominantly mode I cracks. These research findings provide valuable insights to advance understanding of the mechanical

response and crack propagation evolution of surrounding rock in roadway engineering.

KEYWORDS

sandstone, digital image correlation, strain field, displacement field, crack propagation

1 Introduction

With the development of the national economy, population growth, and national security needs, seeking energy and space from the depths of the earth is the only way to solve the basic problems of human resources, energy, and living space. The mining of deep resources and energy (Xie et al., 2015) and the development and utilization of deep underground spaces (such as underground transportation (Zhang et al., 2024), underground *in situ* laboratories, etc.) are often accompanied by rock dynamic disasters with strong destructive power (Zhang et al., 2023; Pan, 2011), such as rock burst, coal and gas outburst, mining earthquake, and large deformation of surrounding rock in tunnels, which seriously restrict the development of resources and energy and future sustainable development in China. Therefore, deep rock mechanics has become a focus of research both domestically and internationally (Kong B. et al., 2025; Sellers and Klerck, 2000; Kong X. G. et al., 2025; Qian, 2004; Kong et al., 2024a; Diering, 1997; Vogel and Andrast, 2000). Studying the deformation and failure mechanisms of rocks at the macro and micro scales has important practical value and theoretical significance for enhancing people's understanding of deep engineering geological hazards and taking corresponding prevention and control measures.

Digital image correlation (DIC) is a widely used non-contact optical digital technology for measuring material deformation, first proposed by Peters and Ranson in the 1980s (Zhou et al., 2024). Subsequently, domestic and foreign scholars conducted in-depth research on the surface displacement field and strain field of rock materials during deformation and fracture processes using DIC technology. Kahn-Jetter and Chu (1990) used digital image correlation technology to measure three-dimensional displacement fields, while Wang et al. (1990) used laser speckle interferometry to study the changes in the rock fracture process zone. Mora et al. (1998), Kwan et al. (1999), Chermant et al. (2001), Liu et al. (2024) et al. have conducted research on the application of DIC in the field of civil engineering, analyzing the distribution characteristics of aggregates and crack propagation in concrete. Yu et al. (2006) introduced DIC technology into the RFPA system and established a method for analyzing the failure process of rock microstructure. Nguren et al. (2011) extended digital image recognition to identify discontinuous displacement characteristics during soft rock fracture processes, while Zhang and Jian, 2013, Zhou et al., 2023 applied DIC combined with high-speed photography technology to measure surface deformation characteristics and loading rate effects of rock samples during dynamic loading processes. Zhou et al. (2025a) analyzed the surface displacement field, strain field, and surface deformation energy density of red sandstone under uniaxial compression conditions using DIC technology. Yamaguchi (2012) analyzed the displacement and image speckle distribution characteristics during the deformation process of small-scale samples, Chen et al. (2023a) analyzed the stress intensity factor characteristics of rocks using mathematical speckle techniques, Zhuo et al. (2013) studied the sliding cooperative displacement characteristics of strike slip faults in metastable states using DIC technology, and Ji et al. (2016) obtained the critical deformation field and process zone length of rock fractures through digital images of the sample surface. Kourkoulis et al. (2013), Yu et al. (2019), Xu et al. (2020), Ren et al. (2022) conducted full field DIC experiments on Brazilian splitting and delamination of concrete under different loading boundary conditions, and analyzed the characteristics of full field deformation and local failure. Zhou et al. (2025b), Zhao et al. (2015), Cao et al. (2016), Yin et al. (2020), Kong et al. (2024b), Li et al. (2023) et al. established a quantitative relationship between crack propagation length and damage based on geometric damage theory, and constructed a rock crack propagation damage evolution equation. Zhao et al. (2016) used digital image correlation technology to systematically study the crack propagation law and microscopic damage evolution mechanism of rock like materials containing different pre-set single cracks under uniaxial compression. Chen et al. (2023b) analyzed the deformation characteristics of tunnel surrounding rock based on similar simulated transparent materials. Wang et al. (2021), Fan et al. (2022), Fu et al. (2022) comprehensively used acoustic emission and digital imaging technology to track the entire process of crack propagation in coal samples and granite, and monitored the evolution of crack propagation from acoustic and optical perspectives. Zhao et al. (2021), Zhao et al. (2023) and others conducted dynamic mechanical properties and surface strain field characteristics of fine sandstone under dynamic load and temperature coupling conditions. Huang et al. (2020) constructed a tunnel model with a size of 3 × 2.4 × 0.4 m containing a fault zone, and analyzed the effect of the fault zone on the tunnel using DIC testing technology. Significant strain localization phenomena were observed at the starting position of the fault. Seisuke et al. (2019) analyzed the application requirements of 3D DIC technology in rock failure process, while (Ma et al., 2017) conducted research on the characteristics of fracture strain and displacement field of brittle rocks based on 3D DIC technology.

The above-mentioned research has deepened our understanding of the fracture characteristics of coal rock masses and similar material simulated rock masses under loads (static and dynamic), but it cannot quantitatively determine the stress and type of rock mass crack initiation. Most of these investigations have been limited to descriptions of macroscopic failure patterns or analyses of standard specimens. Notably, there remains a significant research gap in the quantitative study of crack initiation stresses and crack types (such as tensile, shear, or composite) in sandstones containing non-penetrating arched roadways using 2D-DIC technology. Based on this, this paper utilizes 2D-DIC technology to reveal the evolution

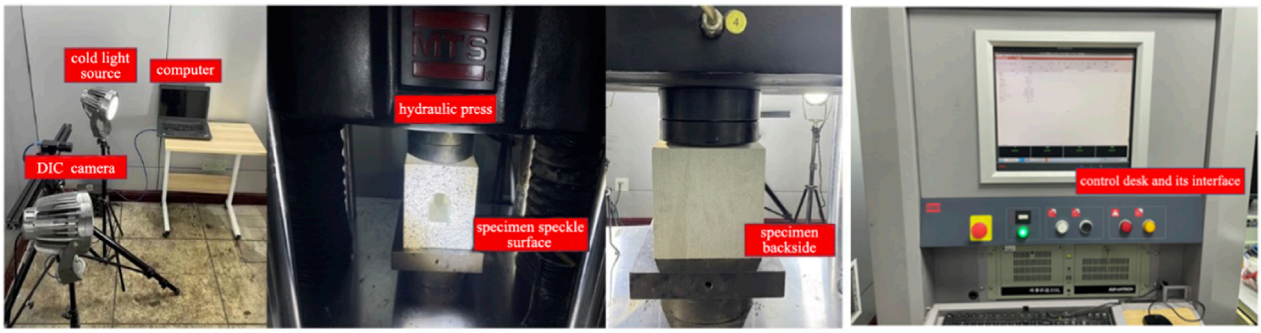

FIGURE 1
Diagram of the experimental system.

characteristics of the principal strain of fractures in roadway rock, calculates the initiation stress and type of each fracture through correlation calculations, and analyzes the horizontal displacement and strain evolution process of the rock mass. This can determine the tensile-shear properties of cracks during the sample loading process. The study provides theoretical and experimental foundations for the health monitoring and damage assessment of coal-rock roadways.

2 Experimental system and scheme

2.1 Experimental equipment

The experimental equipment used in this study includes two parts: 1) data acquisition system; 2) Loading system (MTS C64.605 hydraulic testing machine). Uniaxial compression tests were conducted in force control mode at a constant loading rate of 500 N/s. This loading rate was selected in accordance with recommendations from the International Society for Rock Mechanics (ISRM) to ensure failure of sandstone specimens typically occurred within 5–10 min. This duration is critical for capturing the complete crack initiation and propagation process using the DIC system, which was configured to acquire data at a rate of one frame per second. The data acquisition system includes: image acquisition equipment (CCD camera), cold light source, and data processing equipment. Refer to Figure 1 for details.

2D-DIC technology is used to monitor the crack propagation and damage deformation of rock samples, and system calibration is required before failure. The 2D-DIC system utilized a CCD camera with a resolution of 1,200 × 1,600 pixels. The following procedure and parameters were applied: 1) Speckle treatment: A high-contrast, random speckle pattern was created on the sample surface using matte white spray paint as the background and black ink for the speckles. The average speckle size was controlled to be three to five pixels to optimize the digital correlation accuracy; 2) System Setup and Calibration: The image acquisition device was positioned facing the sample surface. System calibration was performed using a 12 × 9 dot calibration target with a dot spacing of 10 mm. The mean calibration residual was less than 0.03 pixels, ensuring precise measurement. Connect the image acquisition device and data processing device, turn on the data acquisition device, and preheat the device for 10 min; 3) Image Acquisition: The CCD camera acquisition frequency was set to one frame/s. Computer software was used to adjust the exposure and perform light source compensation to ensure consistent image quality; 4) DIC Analysis Parameters: The post-processing analysis was conducted using a subset size of 29 pixels and a step size of five pixels. This parameter set provides a good balance between capturing the fine details of the deformation field and maintaining computational stability. After the adjustment is completed, conduct the experiment.

2.2 Samples preparation

In this experiment, uniformly dense yellow sandstone with a uniaxial compressive strength of about 30 MPa was selected as the material. Standard cubic specimens with dimensions of 150 mm × 150 mm × 150 mm were prepared according to the rock mechanics specification. All specimens were stored and tested under natural dry conditions (laboratory environment maintained at approximately 20 °C and 30%–40% relative humidity) to eliminate the influence of moisture content on the mechanical properties.

The arched roadway was machined using a precision diamond wire saw. A low cutting speed and continuous coolant supply were employed throughout the process to prevent thermal cracking and minimize the introduction of micro-fractures along the roadway boundary.

The front surface of the specimen (designated for DIC observation) was then carefully ground and polished to create a flat and uniform surface, which is crucial for ensuring the accuracy of the subsequent DIC measurements.

Finally, a high-contrast, random speckle pattern was applied to this prepared surface using matte white spray paint and black ink for DIC analysis. A semi-through arch-shaped roadway with a width of 50 mm, height of 52.5 mm, and depth of 75 mm was thus created. Refer to Figure 2 and Table 1 for details.

2.3 Principles of DIC technique

The principle of DIC is to record speckle images of the specimen surface using a CCD camera and track the gray value changes of pixel points to obtain displacement values based on the assumption of gray value invariance. The gray value invariance assumption states

FIGURE 2
Yellow sandstone specimen drawing.

TABLE 1 Parameters of yellow sandstone specimens.

Specimen No	Size/mm × mm × mm	Uniaxial loading rate/N*S^{-1}	Uniaxial compressive strength/MPa	Average compressive strength/MPa
1	150 × 148.6 × 149	500	15.68	15.96
2	151.4 × 151.7 × 150.2		16.17	
3	149 × 148.2 × 149		16.02	

that the gray value of tracked pixel points does not change before and after deformation.

Before performing image correlation calculations, suitable algorithms need to be selected. Most commonly used 2D-DIC algorithms are based on displacement parameters (Meng, 2005), establishing the mapping relationship between pixel points on pre-deformation and post-deformation images. The displacement *(u, v)* of a pixel point *(x, y)* on the pre-deformation image corresponds to the point *(x′, y′)* on the post-deformation image, where $x' = x + u$ (Formula 1) *and* $y' = y + v$ (Formula 2). After establishing the mapping relationship, a correlation formula is selected to calculate the correlation coefficient of a subregion between pre-deformation and post-deformation images. The subregion with the highest correlation coefficient is considered the best match, and displacement and other deformation quantities can be obtained, as shown in Figure 3.

$$x' = x + u(x, y) \tag{1}$$

$$y' = y + v(x, y) \tag{2}$$

3 Analysis of test results

3.1 Stress-strain curve of the specimen under loading

Taking the No. 2 yellow sandstone specimen as an example, analyzing the typical stress-strain comparison relationship of rock specimens under uniaxial compressive loading conditions is shown in Figure 4, and the deformation and destruction process of the specimen is mainly divided into four stages:

1. Initial compaction stage I (horizontal stress 0–15%): the stress of the specimen at this stage rises slowly with the increase of strain, and the yellow sandstone specimen rises more slowly than the white sandstone specimen, which indicates that the applied prestress makes the original crack in the specimen compacted and closed, and the strain increases rapidly, and the stress-strain curve shows an up-concave type, and the surface of the yellow sandstone specimen is more fragile, and its strain increases more rapidly.
2. Linear elasticity stage II; (15%–70% of the peak stress): stress increases linearly with strain, and strain rate accelerates. During this stage, some micro-fractures are generated, see Figure 4, accompanied by the closure of original cracks, leading to a steady increase in strain.
3. Plastic deformation stage III (horizontal stress 70%–100%): in this stage, the specimen micro-fracture develops rapidly, and a large number of cracks converge into macroscopic cracks. The accelerated accumulation of strain increases the degree of damage to the rock sample and produces irreversible damage internally. The peak stress of yellow sandstone is about 16 MPa.
4. Post-peak failure stage IV: In this stage, the stress drops abruptly, and the bearing capacity is greatly reduced. Internal cracks propagate rapidly and interconnect, forming a macroscopic rupture surface and leading to the final failure of the specimen.

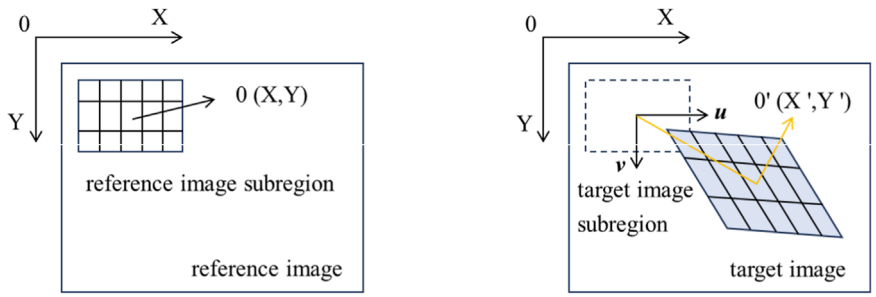

FIGURE 3
DIC capture image schematic.

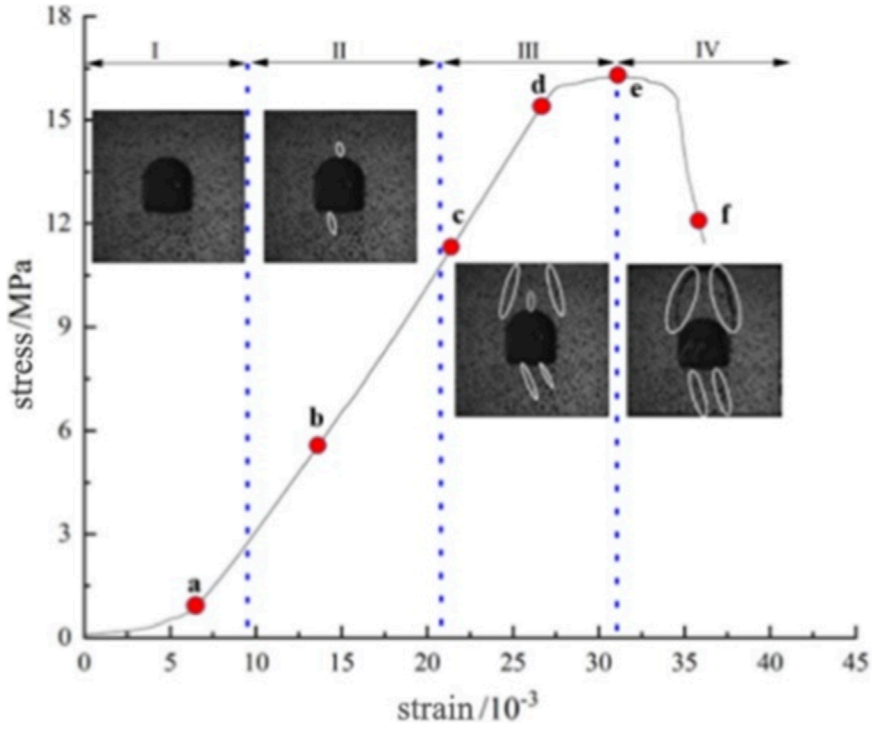

FIGURE 4
Stress-strain relationship curve of yellow sandstone specimen.

3.2 Digital image correlation analysis

Combined with the characteristics of the stress-strain curves of the specimens, the pictures were selected with the loading stage as a reference, corresponding to the full-field displacement and strain clouds along the X-direction (perpendicular to the loading direction) at the six points a, b, c, d, e, and f in Figure 4, respectively.

Figure 5 shows the full-field displacement cloud diagram in X direction (vertical load direction) under different load levels, and the displacement to the right side of the crack is positive, and to the left side is negative. It shows that on the left side of the roadway, the specimen surface is peeled off along the damage points ③ and ⑤, and on the right side of the roadway, the specimen surface is peeled off along the damage points ② and ④, and the absolute value of the full-field displacement gradually increases with the increase of the load. Before the load level is 70%, the displacement increases relatively insignificantly, with a maximum displacement of about 0.3 mm, and then, in the stage of accelerated crack expansion, the displacement increases rapidly, with a maximum displacement of 0.4 mm at the load level of 100%, which can even increase to 1 mm instantaneously after brittle damage.

In the compaction stage, the specimen is under the action of load, the internal gap of the rock specimen is continuously compacted, the displacement field of the specimen is increasing and tends to be stabilized, and the displacement field shows obvious changes, see the displacement cloud diagram corresponding to the point a in Figure 5. During the linear elastic stage, the internal stress of the specimen accumulates under loading. Stress concentration

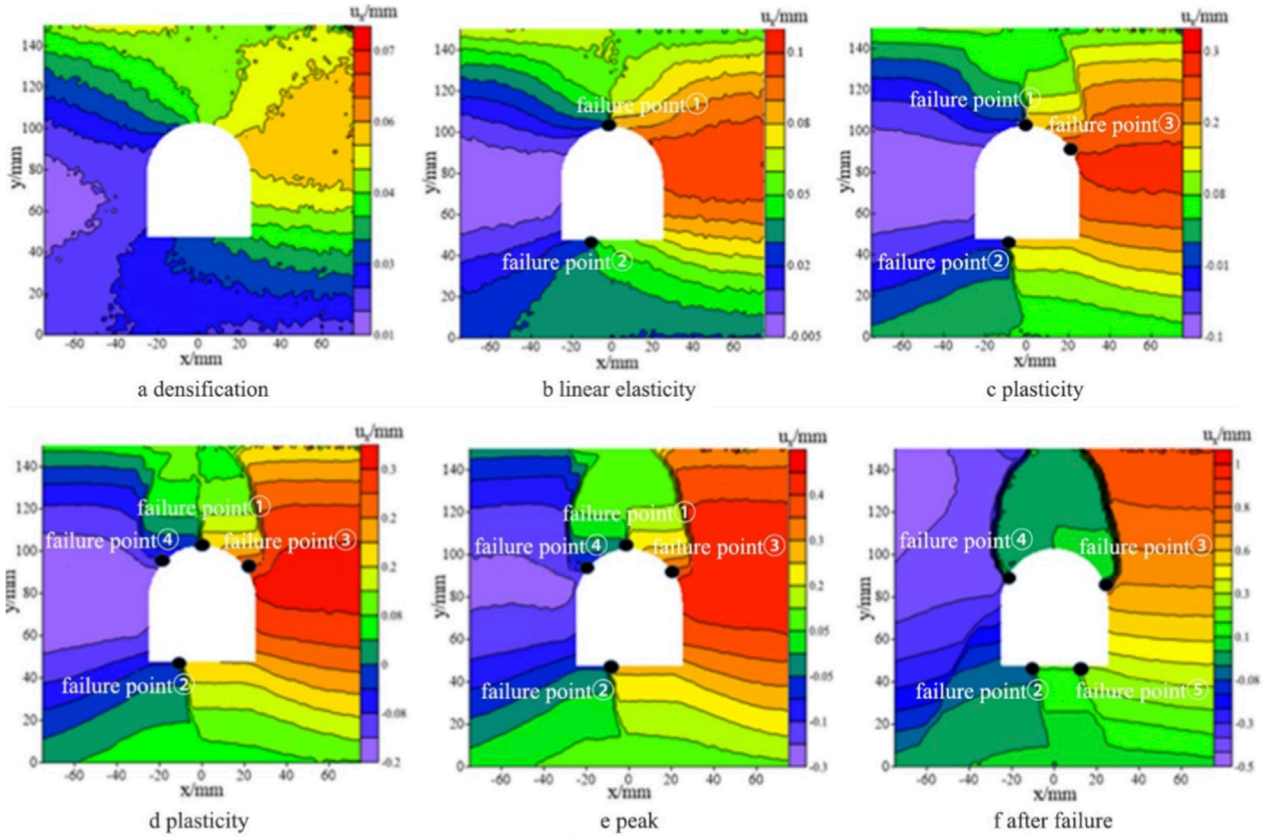

FIGURE 5
Full-field displacement cloud of X direction (vertical load direction) at different load levels.

occurs in the surrounding rock of the roadway, leading to a significant increase in displacement. Damage points ① and ② appear, where cracks initiate and develop. Macro-deformation begins to emerge in the later part of this stage, which corresponds to the displacement cloud image at point b in Figure 5. During the plastic stage, the roadway undergoes gradual damage. Cracks initiated in the surrounding rock, particularly at the roof, continue to propagate, ultimately leading to the collapse of the roadway. Concurrently, distinct strain concentration bands become visible on all sides (left, right, top, and bottom) of the roadway. These bands progressively localize (become more refined and intense), eventually giving rise to obvious macroscopic cracks on the rock surface. The surface of the rock produced obvious macrocracks along the damage points ①,②, ③, ④ to form four macrocracks, the model surface appears to develop cracks and the phenomenon of block detachment, the maximum displacement at this time reached 0.4 mm, but the rock body still maintains the integrity of the stage corresponds to the displacement field cloud diagrams corresponding to the points c, d in Figure 5. In the post-damage stage, the roadway model has been completely damaged, the surface blocks collapsed, and the surrounding rock of the sandstone roadway is seriously destabilized. Moreover, new cracks are formed along the damage point ⑤, and the maximum displacement reaches 1 mm, which corresponds to the displacement field cloud image of point f in Figure 5.

Figure 6 shows the full-field strain cloud in the x-direction (vertical loading direction) under different loading levels, and the displacement of the crack is positive to the right and negative to the left. It shows that the strain change along the x-direction of the specimen gradually increases with the increase of loading time. Before the loading level is 70%, the strain increases relatively insignificantly with a maximum strain of about 0.01, after that, in the accelerated crack expansion stage, the strain increases rapidly, reaching a maximum value of 0.03 at the 100% load level at the loading level of 100%, and it can even increase to 0.06 instantaneously after brittle damage.

As the load increases, the stress within the specimen rises and energy accumulates. When the stress reaches the cracking threshold, the evolution of local strain becomes highly pronounced. Subsequently, cracks within the specimen propagate rapidly, leading to macroscopic deformation. In the plastic phase, the specimen channel is damaged, and the cracks in the channel perimeter rock continue to expand, and cracks are formed along the cracks at the damage points, and this phase corresponds to the strain field cloud diagrams corresponding to points c and d in Figure 6. The strain gathering near the crack at the peak stress is obvious, and the peripheral rock at the top of the roadway collapses in a large area, and the strain value reaches 0.03, and this stage corresponds to the strain field cloud diagram corresponding to point e in Figure 6. In the post-peak stage, the specimen is basically completely damaged,

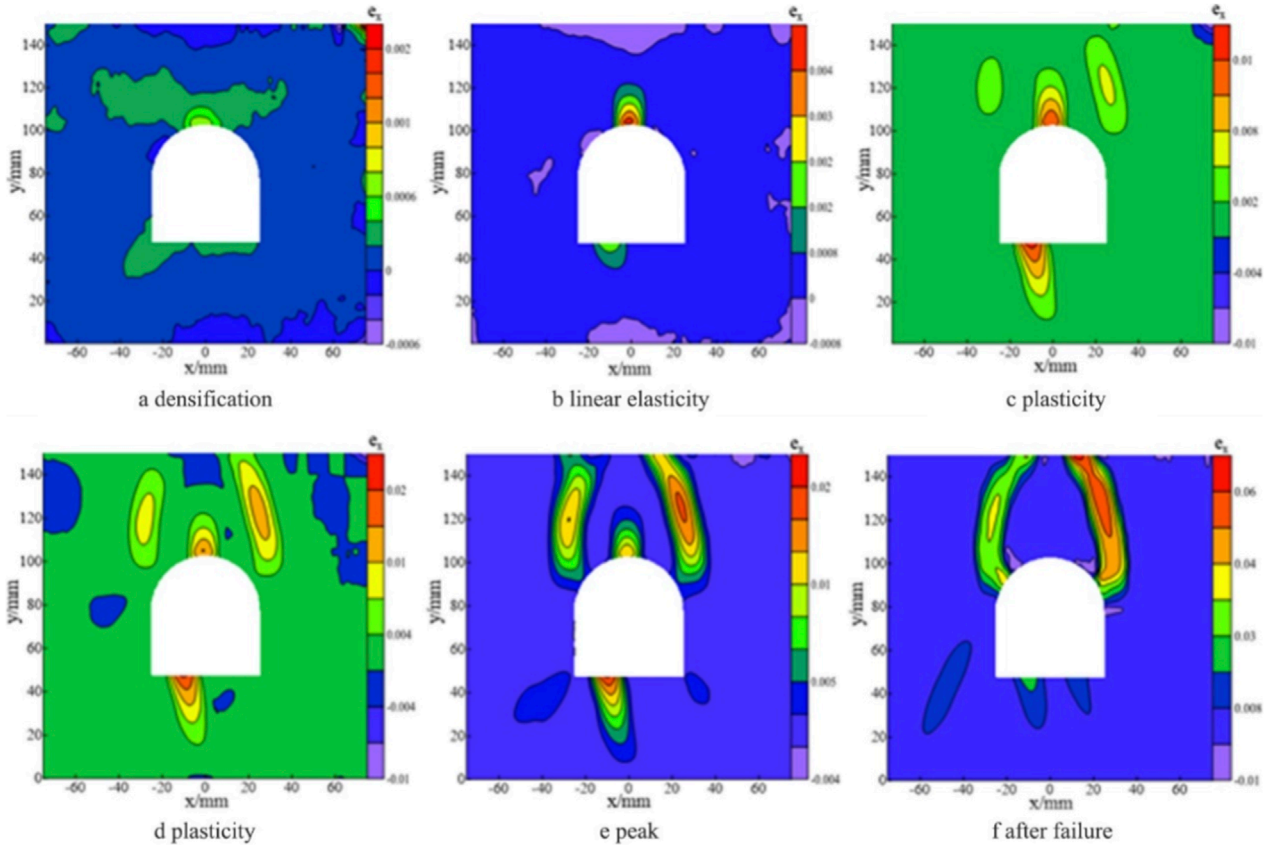

FIGURE 6
Full-field strain cloud in the X direction (vertical load direction) at different load levels.

the surrounding rock of the roadway is seriously destabilized, and the strain reaches about 0.06, and this stage corresponds to the strain field cloud diagram corresponding to point f in Figure 6.

4 Analysis of crack propagation characteristics based on DIC

In general, the damage evolution process of rocks is often described in terms of crack propagation characteristics. The evolution of principal strains of individual cracks captured using 2D-DIC technology can be used to depict the mechanism of rock damage evolution.

4.1 Evolving characteristics of principal strains in crack propagation

Through the principal strains in cracks, the stage characteristics of apparent crack initiation, development, and propagation in rocks can be reflected. This study monitored the dynamic evolution process of principal strains on the surface of rock specimens under uniaxial compression conditions using DIC technology. Cracks in the process of initiation and propagation cause localized strain accumulation, which differs significantly from other regions of uniform deformation, referred to as strain jump points. Using MatchID-2D software, the strain values at local strain concentration points were statistically analyzed across a two-dimensional spatial distribution. For each crack, multiple analysis points were uniformly selected along its path. The maximum principal strain data at each point were extracted, and the average value of the maximum principal strain corresponding to multiple points at each loading time was taken as the maximum principal strain of the entire crack. There were a total of five main cracks in the rock specimen, as shown in Figure 7, and the evolution process of principal strains in these cracks is illustrated in Figure 8.

To clearly describe the evolution process of the maximum principal strain in cracks, it can be roughly divided into three stages. In the first stage, the change in the maximum principal strain of the crack is very small, and the curve is approximately horizontal, indicating that the development of surface cracks in the sandstone sample is not significant. This stage roughly corresponds to the compaction stage and the linear elastic deformation stage in the classic rock mechanics curve. At this stage, crack 1, crack 3, and crack 4 show a noticeable increase in the maximum principal strain, with the corresponding time points at around 610s, 170s, and 240s, respectively.

In the second stage, the principal strain in the crack shows a slow accelerating trend. DIC technology captures the initiation and slow expansion of microcracks on the surface of the rock sample that

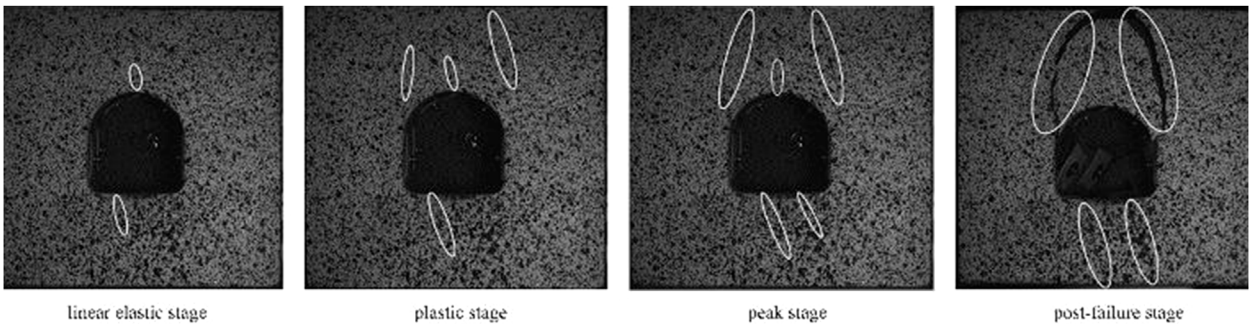

FIGURE 7
Crack distribution of rock samples under different loads.

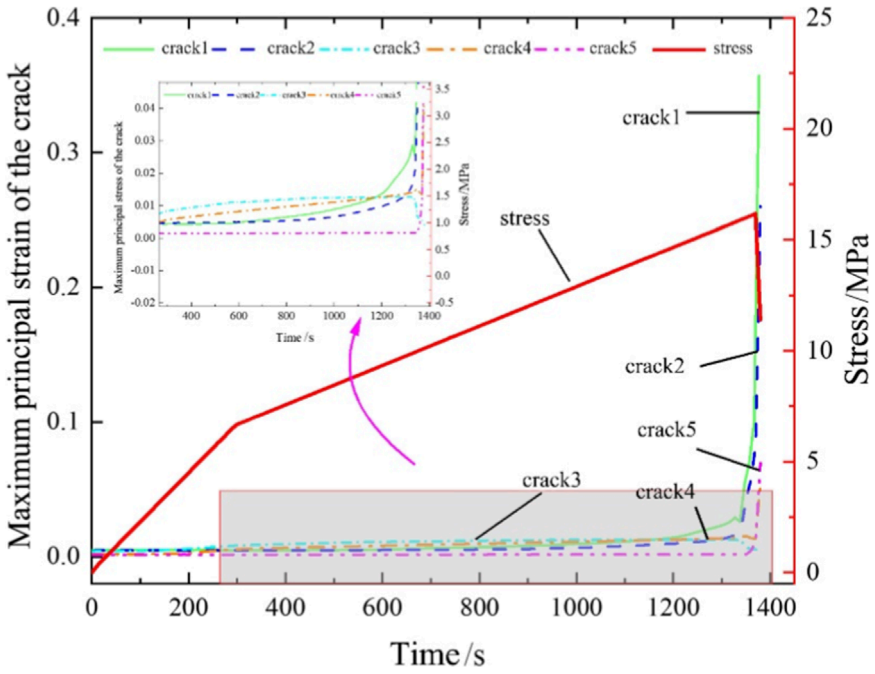

FIGURE 8
Evolution characteristics of maximum principal strain of cracks.

are difficult to identify with the naked eye. The rock mass remains partially intact, corresponding to the plastic deformation stage in the stress-strain curve. The reason for this phenomenon is that certain parts of the rock mass have lower strength, and microcracks appear first. As the specimen is loaded, the internal cracks continue to expand, gradually forming through-cracks and ruptured surfaces. Visible cracks begin to appear on the surface of the specimen. At this stage, there is a significant increase in the maximum principal strain of crack 2, with the corresponding time point at around 810s. In the third stage, the principal strain in the cracks exhibits an accelerating growth with an increasing acceleration. The apparent cracks on the rock sample show accelerated extension and expansion. Macroscopic cracks form and continue to propagate until the rock sample experiences unstable failure. This is because the coal body has essentially lost its load-bearing capacity, leading to failure and extension into the rock mass. At around 1365s, there is a sudden increase in the maximum principal strain of cracks 1, 2, 4, and 5. It is worth noting that crack three experiences a significant decrease in the maximum principal strain during peak stress. This is due to the expansion of cracks one and two during the failure of the rock sample, causing compression closure of crack 3, as shown in Figure 8. There is a significant difference in the strain distribution between the upper/lower sides and the left/right sides of the cavity. The maximum principal strain at the top and bottom of the cavity is typically below 0.005, which is much smaller than that on the sidewalls. For instance, at peak stress, the average maximum principal strain for cracks on the left side (Crack 1 and 4) reached approx. 0.019, while those on the right side (Crack 2 and 5) reached approx. 0.018. The close agreement in these values quantitatively demonstrates a near-symmetric strain state prior to ultimate failure.

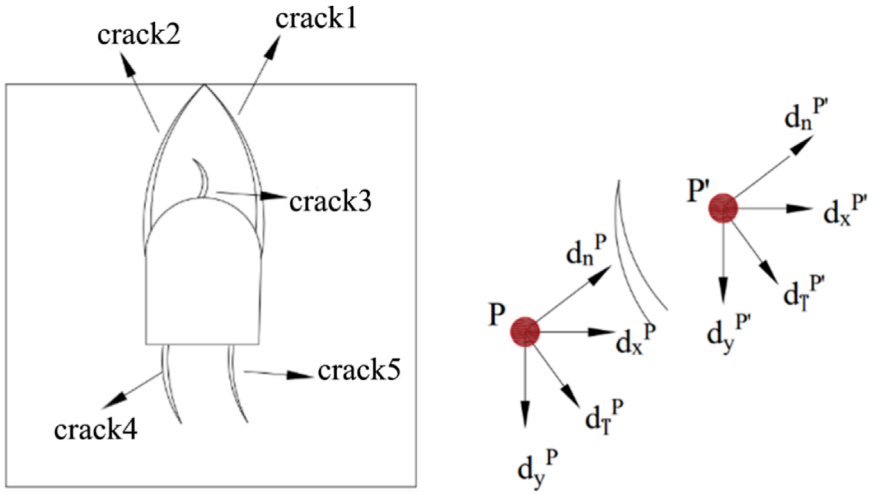

FIGURE 9
Schematic diagram of crack angle.

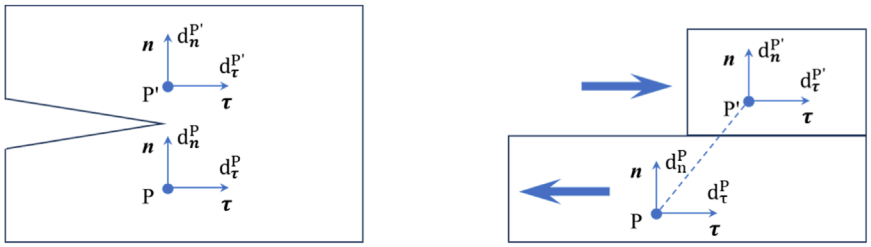

FIGURE 10
Type I crack and type II crack deformation mode in fracture mechanics theory.

Therefore, DIC technology can effectively monitor the initiation and extension trends of cracks, which is of great significance for assessing the stability of rocks.

4.2 Crack initiation stress and classification

In previous studies, strain gauges were typically attached to the surface of the specimen to study the fracture process. However, due to the uncertainty in the initiation position and angle of cracks, this method is complex during experimental preparation, making it difficult to determine the bonding position of the strain gauges prior to the experiment. In contrast, Digital Image Correlation (DIC) analysis can overcome these issues. Using 2D-DIC technology, multiple monitoring points P and their symmetrical points P′ are selected on both sides of each crack initiation position on the speckle surface of the rock specimen. The displacement values of these monitoring points along the vertical and horizontal directions of the specimen are obtained. By using Equations 3–6, the relative displacements of P and P′ along the normal and tangential directions of the crack are obtained. The contrasting analysis of dn and dγ allows for the determination of the crack type (Liu et al., 2021), as shown in Figure 9.

$$dn^p = dx^p \cos\alpha + dy^p \sin\alpha \tag{3}$$

$$d\tau^p = -dx^p \sin\alpha + dy^p \cos\alpha \tag{4}$$

$$dn^{p'} = dx^{p'} \cos\alpha + dy^{p'} \sin\alpha \tag{5}$$

$$d\tau^{p'} = -dx^{p'} \sin\alpha + dy^{p'} \cos\alpha \tag{6}$$

In the above equations, dn^P and $d\tau^P$ represent the relative displacements of monitoring point P along the normal and tangential directions of the crack, respectively. $dn^{P'}$ and $d\tau^{P'}$ represent the relative displacements of monitoring point P′ along the normal and tangential directions of the crack, respectively. dx^P and dy^P represent the relative displacements of monitoring point P along the horizontal and vertical directions of the specimen obtained through digital image correlation (DIC) processing. Similarly, $dx^{P'}$ and $dy^{P'}$ represent the relative displacements of monitoring point P′ along the horizontal and vertical directions of the specimen obtained through DIC processing. α represents the angle between the local coordinate system of the crack and the global coordinate system. The local coordinate system of the crack consists of two directions: along the normal and tangential directions of the crack. The global

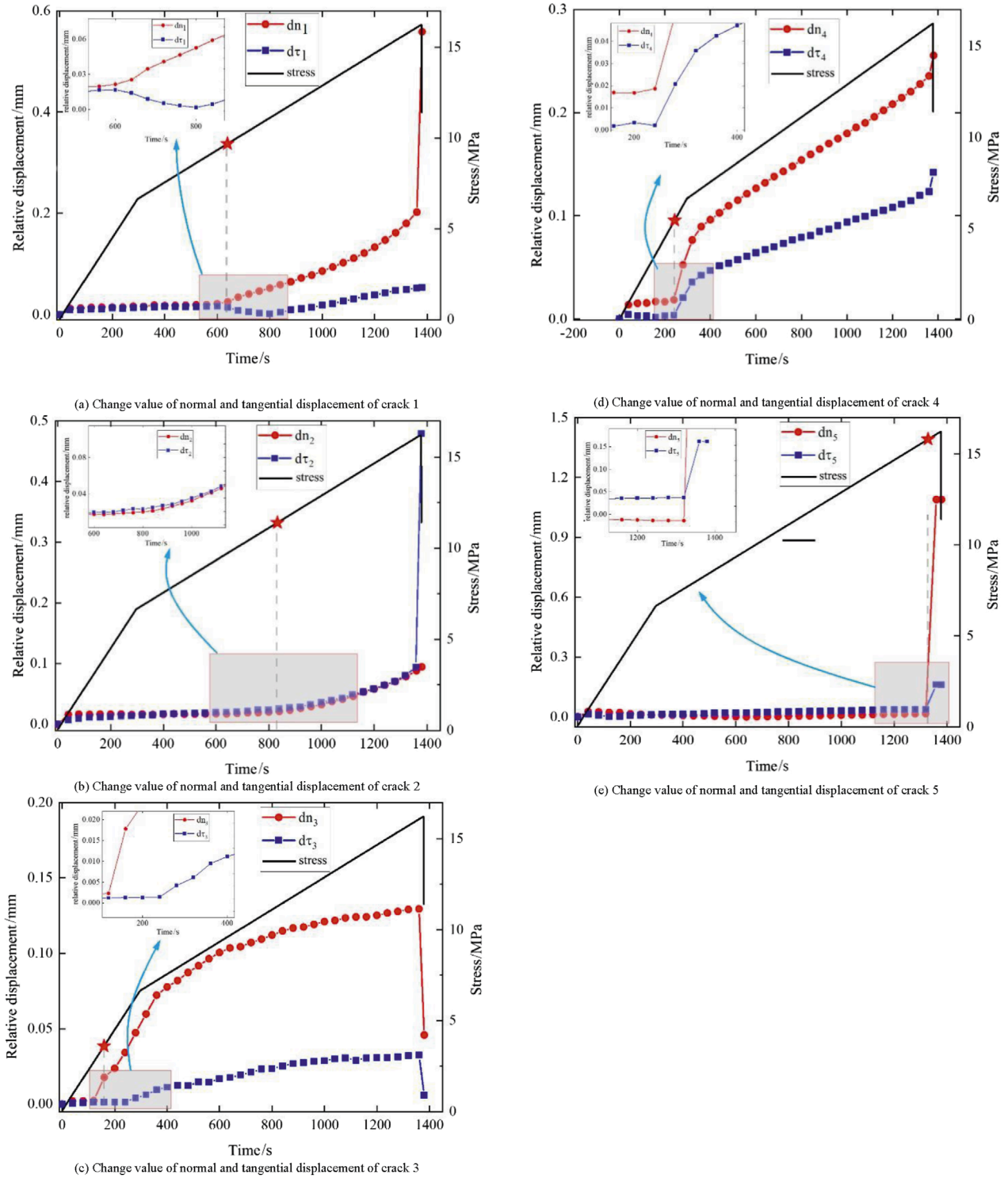

FIGURE 11
Displacement values of different crack normal and tangential directions. **(a)** Change value of normal and tangential displacement of crack 1. **(b)** Change value of normal and tangential displacement of crack 2. **(c)** Change value of normal and tangential displacement of crack 3. **(d)** Change value of normal and tangential displacement of crack 4. **(e)** Change value of normal and tangential displacement of crack 5.

coordinate system consists of the vertical and horizontal directions of the specimen, as shown in Figure 9.

Based on the assumption of fracture mechanics, the behavior of cracks initiated under complex stress conditions can be studied by superimposing three basic crack tip deformation modes (Scavia, 1995): Mode I (opening mode), Mode II (sliding mode), and Mode III (tearing mode). Due to the difficulty of implementing DIC (Digital Image Correlation) technique for Mode III cracks, they are

not considered in this study. The criterion for Mode I identification is as follows: When the tensile stress perpendicular to the crack surface exceeds the material strength, a Mode I crack is formed. The top and bottom surfaces of the crack will open, indicating that the normal relative displacement (dn^p') is greater than 0, while the tangential relative displacement is 0. However, achieving zero tangential relative displacement is difficult in practice. Therefore, when the normal relative displacement is much larger than the tangential relative displacement (i.e., $\left\{\left(dn^{p'} - dn^{p} \gg \left|d\tau^{p} - d\tau^{p}\right|\right\}\right)$, it can be determined as a Mode I crack. The criterion for Mode II identification is as follows: When the applied normal or shear stress on the crack surface is zero, the two surfaces will remain in contact, resulting in an approximate zero normal relative displacement. At the same time, shear stress will cause sliding between the upper and lower surfaces of the crack, leading to a positive tangential relative displacement. However, achieving zero normal relative displacement is difficult in practice. Therefore, when the tangential relative displacement is much larger than the normal relative displacement (i.e., $\{\left|d\tau^{p} - d\tau^{p'}\right| \gg \left(dn^{p'} - dn^{p}\right)\}$), it can be determined as a Mode II crack, as shown in Figure 10.

Specific analysis: The approximate initiation time of the first crack can be determined as 610 s, and the corresponding stress value at that time is 9.62 MPa. Therefore, the initiation stress of this crack is 9.62 MPa, as indicated by the star symbol in Figure 11. By analyzing the relationship between the changes in normal direction and tangential direction relative displacements (dn, dτ) at the crack initiation position, it can be observed that both the displacement difference dn and dτ vary. The relative displacement dn is much larger than dτ, indicating that sliding deformation along the shear direction of the crack is the main driving factor for crack initiation. Therefore, it can be determined that the crack initiation type is Mode I, and the corresponding relative displacement dn is 0.0244 mm. The second crack can be approximately determined to have initiated at 810 s. At this time, both the normal and tangential displacements show changes, indicating an initiation stress of 11.23 MPa. Since the normal relative displacement and tangential relative displacement of the crack increase almost simultaneously, it indicates that both opening deformation in the normal direction and sliding deformation in the tangential direction of the crack occur simultaneously. Therefore, it can be determined that the crack initiation type is a mixed Mode I/II crack, with a corresponding relative displacement dn of 0.0244 mm. The third crack can be approximately determined to have initiated at 170 s. At this time, the normal relative displacement has undergone significant changes, corresponding to an initiation stress of 3.94 MPa. The corresponding relative displacement dn at this time is 0.0178 mm. When the specimen is loaded to 280 s, the tangential displacement undergoes significant changes. Since the normal relative displacement of this crack is much larger than the tangential relative displacement, it indicates that opening deformation in the normal direction dominates. Therefore, this crack can be determined as a mixed Mode I crack. The fourth crack can be approximately determined to have initiated at 240 s, corresponding to an initiation stress of 5.29 MPa. Since the normal relative displacement and tangential relative displacement of this crack increase almost simultaneously, it can be determined as a mixed Mode I/II crack, with a corresponding dn of 0.0186 mm. The fifth crack can be approximately determined to have initiated at 1,365 s, with an initiation stress of 15.97 MPa. Similar to the second and fourth cracks, it is considered a mixed Mode I/II crack, with a corresponding dn of 0.0152 mm. Therefore, it can be concluded that in the case of uniaxial loading on the sandstone arch roadway, the cracks are mainly Mode I cracks and mixed Mode I/II cracks, with crack initiation occurring when the relative displacement dn reaches approximately 0.02 mm.

5 Conclusion

This study uses DIC technology to experimentally investigate the macro- and micro-scale stress-strain characteristics during the uniaxial compression failure process of yellow sandstone containing arched tunnels. The variation patterns of strain and displacement fields at different stress stages, as well as the evolution of crack propagation, are analyzed. The crack propagation mechanism of yellow sandstone specimens containing arched tunnels under uniaxial compression is elucidated.

1. The failure process of the sandstone specimen with an arched roadway is delineated into four distinct stages: initial compaction, linear elasticity, plastic deformation, and instability failure. More importantly, the quantitative analysis reveals that the accelerated crack growth stage (plastic deformation) commences at approximately 70% of the peak stress. This critical stress threshold provides a valuable indicator for early warning of surrounding rock instability in practical engineering.
2. The evolution of displacement and strain fields, captured by DIC, demonstrates that significant deformation localization occurs prior to macroscopic cracking. This finding underscores the capability of full-field measurement techniques like DIC to identify potential failure zones that are not yet visible, offering a proactive approach for stability assessment beyond traditional monitoring methods.
3. Using the DIC technique, the strain evolution process of each crack during loading is derived. The results show that quantitative comparison at peak stress shows that the maximum principal strain on the left side and the right side reached highly comparable magnitudes, with a relative difference of only about 5%. The strain distributions on the left and right sides of the roadway are significantly larger than those on the upper and lower sides, exhibiting a certain symmetry.
4. The relative tangential and normal displacements of each crack are obtained by determining the crack initiation angle and the horizontal and vertical displacements at two points on either side of the crack initiation position. Combined with difference calculations, these values are used to derive the shear properties of the cracks and their corresponding initiation times and stresses. Under uniaxial loading, the cracks in yellow sandstone specimens containing arched roadways are primarily Mode I and mixed Mode I/II cracks. Cracking initiates when the relative displacement d_n reaches approximately 0.02 mm. This quantitative parameter can serve as a potential micro-mechanical criterion for predicting the onset of damage in similar geological materials.

Data availability statement

The original contributions presented in the study are included in the article/supplementary material, further inquiries can be directed to the corresponding authors.

Author contributions

YY: Writing – original draft, Writing – review and editing. YZ: Writing – original draft, Writing – review and editing. MZ: Writing – original draft, Writing – review and editing.

Funding

The authors declare that no financial support was received for the research and/or publication of this article.

Conflict of interest

Author YY was employed by Henan Pingmei Shenma Liangbei No.2 Mine Industry Co., Ltd. Author MZ was employed by Huaneng Xindian Power Generation Co., Ltd.

The remaining author declares that the research was conducted in the absence of any commercial or financial relationships that could be construed as a potential conflict of interest.

Generative AI statement

The authors declare that no Generative AI was used in the creation of this manuscript.

Any alternative text (alt text) provided alongside figures in this article has been generated by Frontiers with the support of artificial intelligence and reasonable efforts have been made to ensure accuracy, including review by the authors wherever possible. If you identify any issues, please contact us.

Publisher's note

References

Cao, W. G., Zhang, C., He, M., and Liu, T. (2016). Statistical damage simulation method of strain softening deformation process for rocks considering characteristics of void compaction stage. *Chin. J. Geotechnical Eng.* 38, 1754–1761. doi:10.11779/CJGE201610002

Chermant, J. L., Chermant, L., Coster, M., Dequiedt, A. S., and Redon, C. (2001). Some fields of applications of automatic image analysis in civil engineering. *Cem. and Concr. Compos.* 23, 157–169. doi:10.1016/s0958-9465(00)00059-7

Chen, Y., Suo, J., Li, J., Wei, F., Cao, H. H., and Sun, H. Z. (2023a). Active–passive remote sensing identification of underground coal fire zones with joint constraints of temperature and surface deformation time series. *IEEE Journal of Selected Topics in Applied Earth Observations and Remote Sensing* 17, 894–915.

Chen, Y., Li, J., Li, H. Z., Gao, Y., Li, S., and Chen, S. (2023b). Revealing land surface deformation over the yineng backfilling mining area, china, by integrating distributed scatterer sar interferometry (Ds Insar) and a mining subsidence model. *IEEE Journal of Selected Topics in Applied Earth Observations and Remote Sensing* 16, 3611–3634. doi:10.1109/JSTARS.2023.3250419

Diering, D. H. (1997). Ultra-deep level mining: future requirements. Journal of the South African Institute of Mining and Metallurgy, 97(6), 249–255.

Fan, J., Zhu, X., Hu, J. W., Tang, Y., and He, C. L. (2022). Experimental study on crack propagation and damage monitoring of sandstone using three-dimensional digital image correlation technology. *Rock Soil Mech.* 43, 1009–1019. doi:10.16285/j.rsm.2021.1132

Fu, S. Y., Li, H. B., and Li, X. F. (2022). Research on the range of fracture process zone of granite based on DIC and acoustic emission. *Chin. J. Rock Mech. Eng.* 41, 2497–2508. doi:10.13722/j.cnki.jrme.2022.0156

Huang, F., Wu, C. Z., Ni, P. P., Wan, G. Q., Zhang, A. C., Jang, B. A., et al. (2020). Experimental analysis of progressive failure behavior of rock tunnel with a fault zone using non-contact DIC technique. *Int. J. Rock Mech. Min. Sci.* 1, 104355. doi:10.1016/j.ijrmms.2020.104355

Ji, W. W., Pan, P. Z., Miao, S. T., Su, F. S., and Du, M. P. (2016). Fracture characteristics of two types of rocks based on digital image correlation. *Rock Soil Mech.* 37, 2299–2305. doi:10.16285/j.rsm.2016.08.023

Kahn-Jetter, Z. L., and Chu, T. C. (1990). Three-dimensional displacement measurements using digital image correlation and photogrammic analysis. *Exp. Mech.* 30, 10–16. doi:10.1007/bf02322695

Kong, X. G., Lin, X., Cai, Y. C., Chen, L., Hu, J., Zhou, Y. X., et al. (2024a). Effects of pore characteristics on CO2 adsorption performance of coal slime with different metamorphic degrees. *J. Environ. Manag.* 368, 122094. doi:10.1016/j.jenvman.2024.122094

Kong, X. G., Zhan, M. Z., Lin, H. F., Cai, Y. C., Ji, P. F., He, D., et al. (2024b). Time-varying characteristics of acoustic emission and fractals based on information dimension during structural failure of coal subjected to uniaxial compression. *Measurement* 236, 115088. doi:10.1016/j.measurement.2024.115088

Kong, B., Wan, H. J., Zhu, S. X., Zhang, W. R., Song, S. L., Zhang, X. L., et al. (2025a). Development and implementation of an intelligent early warning system for preventing environmental pollution from coal spontaneous combustion. *Green Smart Min. Eng.* 2, 313–329. doi:10.1016/j.gsme.2025.09.005

Kong, X. G., Zhang, H., Ma, Y. K., Liu, T., Zhao, P. X., Muhammad, A., et al. (2025b). Temporal-spatial laws of microseismic events induced by the fracture evolution of overburden strata and the relationship with gas emission during coal mining engineering. *J. Appl. Geophys.* 243, 105965. doi:10.1016/j.jappgeo.2025.105965

Kourkoulis, S. K., Markides, C. F., and Chatzistergos, P. E. (2013). The standardized Brazilian disc test as a contact problem. *Int. J. Rock Mech. Min. Sci.* 57, 132–141. doi:10.1016/j.ijrmms.2012.07.016

Kwan, A. K. H., Mora, C. F., and Chan, H. C. (1999). Particle shape analysis of coarse aggregate using digital image processing. *Cem. and Concr. Res.* 29, 1403–1410. doi:10.1016/s0008-8846(99)00105-2

Li, S. N., Xiao, J., Li, Y., Liu, X. X., Liang, Q., Chang, J., et al. (2023). A new damage constitutive model of rock considering microscopic crack growth. *Chin. J. Rock Mech. Eng.* 42, 640–648. doi:10.13722/j.cnki.jrme.2022.0364

Liu, L. W., Li, H. B., Li, X. F., Wu, D., and Zhang, G. K. (2021). Underlying mechanisms of crack initiation for granitic rocks containing a single pre-existing flaw: insights from digital image correlation (DIC) analysis. *Rock Mech. Rock Eng.* 54, 857–873. doi:10.1007/s00603-020-02286-x

Liu, X., Zhou, X., Zheng, Z., Zhang, H., Gu, Z., Zhang, S. Q., et al. (2024). Compound disaster characteristics of rock burst and coal spontaneous combustion in island mining face: a case study. *Case Studies in Thermal Engineering*, 105240. doi:10.1016/j.csite.2024.105240

Ma, Y. S., Chen, W. Z., Yang, D. S., Yang, J. P., and Gong, Z. (2017). Experimental study of brittle rock failure based on three-dimensional digital image correlation technique. *Rock Soil Mech.* 38, 117–123. doi:10.16285/j.rsm.2017.01.015

Meng, L. B. (2005). *Study and application of digital speckle correlation method*. Beijing: Tsinghua University.

Mora, C. F., Kwan, A. K. H., and Chan, H. C. (1998). Particle size distribution analysis of coarse aggregate using digital image processing. *Cem. and Concr. Res.* 28, 921–932. doi:10.1016/s0008-8846(98)00043-x

Nguren, T. L., Hall, S. A., Vacher, P., and Viggiani, G. (2011). Fracture mechanisms in soft rock:identification and quantification of evolving displacement discontinuities by extended digital image correlation. *Tectonophysics* 503, 117–128. doi:10.1016/j.tecto.2010.09.024

Pan, Y. S. (2011). Integrated study on compound dynamic disaster of coal-gas outburst and rock burst. *J. China Coal Soc.* 41, 105–112. doi:10.13225/j.cnki.jccs.2015.9034

Qian, Q. H. (2004). "The key problems of deep underground space development," in *The key technical problems of base research in deep underground space development-the 230th xiangshan science conference*. doi:10.13225/j.cnki.jccs.2015.9034

Ren, H. L., Du, Y. N., and Song, S. Z. (2022). Deformation and failure of concrete splitting based on DIC method. *Chin. J. High Press. Phys.* 36, 91–100. doi:10.11858/gywlxb.20220509

Scavia, C. (1995). A method for the study of crack propagation in rock structures. *Geotechnique* 45, 447–463. doi:10.1680/geot.1995.45.3.447

Seisuke, O., Tang, Y., Xu, J., Peng, S. J., Chen, C. C., and Yan, Z. S. (2019). Application of 3D-DIC system in rock mechanics test. *Rock Soil Mech.* 40, 3263–3273. doi:10.16285/j.rsm.2018.0861

Sellers, E. J., and Klerck, P. (2000). Modelling of the effect of discontinuities on the extent of the fracture zone surrounding deep tunnels. *Tunneling Undergr. Space Technol.* 15, 463–469. doi:10.1016/s0886-7798(01)00015-3

Vogel, M., and Andrast, H. P. (2000). Alp transit-safety in construction as a challenge, health and safety aspects in very deep tunnel construction. *Tunneling Undergr. Space Technol.* 15, 481–484. doi:10.1016/s0886-7798(01)00018-9

Wang, C. Y., Liu, P. D., Hu, R. S., and Sun, X. T. (1990). Study of the fracture process zone in rock by laser speckle interferometry. *Int. J. Rock Mech. Min. Sci. and Geomechanics Abstr.* 27, 65–69. doi:10.1016/0148-9062(90)90010-y

Wang, X. R., Wang, E. Y., Liu, X. F., Li, N., and Zhou, X. (2021). Three-point-bending test of crack propagation and fracture parameters of coal specimens. *Chin. J. Rock Mech. Eng.* 40, 690–702. doi:10.13722/j.cnki.jrme.2020.0736

Xie, H. P., Gao, F., Ju, Y., Gao, M. Z., Zhang, R., Gao, Y. N., et al. (2015). Quantitative definition and investigation of deep mining. *J. China Coal Soc.* 40, 1–10. doi:10.13225/j.cnki.jccs.2014.1690

Xu, J. P., Dong, X. L., Fu, Y. Q., Yu, X. L., and Zhou, F. H. (2020). Experimental analysis of process and tensile strength for concrete Brazilian splitting test with different loading boundaries by DIC method. *Chin. J. Theor. Appl. Mech.* 52, 864–876. doi:10.6052/0459-1879-19-303

Yamaguchi, I. (2012). Speckle displacement and decorrelation in the diffraction and image fields for small object deformation. *Opt. Acta Int. J. Opt.* 28, 1359–1376. doi:10.1080/713820454

Yin, D., Meng, Q. X., Xu, J. R., Shi, A. C., Wu, G. Y., and Xu, W. Y. (2020). Anisotropic elastoplastic constitutive model based on microstructure tensor and its engineering application. *Chin. J. Geotechnical Eng.* 42, 1751–1758. doi:10.11779/CJGE202009020

Yu, Q. L., Tang, C. A., Zhu, W. C., Liu, H. Y., and Liang, Z. Z. (2006). Digital image processing based modeling of rock failure in meso-scale. *Mech. Eng.* 28, 60–64. doi:10.4028/www.scientific.net/KEM.353-358.945

Yu, X. L., Fu, Y. Q., Dong, X. L., Zhou, F. H., Ning, J. G., and Xu, J. P. (2019). Full field DIC analysis of one-dimensional spall strength for concrete. *Chin. J. Theor. Appl. Mech.* 51, 1064–1072. doi:10.6052/0459-1879-19-008

Zhang, Q. B., and Jian, Z. (2013). Determination of mechanical properties and full-field strain measurements of rock material under dynamic loads. *Int. J. Rock Mech. and Min. Sci.* 60, 423–439. doi:10.1016/J.IJRMMS.2013.01.005

Zhang, Z. B., Li, H., Zheng, W. Q., Whattam, S. A., Zhu, Z. J., Jiang, W. C., et al. (2023). Response of Paleogene fine-grained clastic rock deposits in the south Qiangtang Basin to environments and thermal events on the Qinghai-Tibet Plateau. *ACS Omega* 29, 26458–26478. doi:10.1021/acsomega.3c03144

Zhang, Z. B., Sun, J., Ma, Y. K., Wang, Q., Li, H. T., and Wang, E. Y. (2024). Research on the influence mechanism of moisture content on macroscopic mechanical response and microscopic evolution characteristic of Limeston. *Buildings* 14 (2). doi:10.3390/buildings14020469

Zhao, Y. Q., Liu, H. Y., Lü, S. R., and Zhang, L. M. (2015). Damage constitutive model of jointed rock mass based on coupling macroscopic and mesoscopic flaws. *J. Central South University:Science Technol.* 46, 1489–1496. doi:10.11817/j.issn.1672-7207.2015.04.041

Zhao, C., Liu, F. M., Tian, J. S., Matsuda, H., and Morita, C. (2016). Study on single crack propagation and damage evolution mechanism of rock-like materials under uniaxial compression. *Chin. J. Rock Mech. Eng.* 35, 3626–3632. doi:10.13722/j.cnki.jrme.2015.1270

Zhao, E. L., Wang, E. Y., Feng, Z. S. X. J., and Shen, R. X. (2021). Dynamic mechanical characteristics of impact rock under the combined action of different constant temperatures and static and dynamic loads. *Shock. Vib.* 1 (2021), 8484391. doi:10.1155/2021/8484391

Zhao, E. L., Wang, E. Y., and Chen, H. P. (2023). Experiments on the coal measures sandstone's dynamic mechanical parameter characteristics under the combined action of temperature and dynamic load. *Appl. Sci.* 13, 13125. doi:10.3390/app132413125

Zhou, X., Liu, X., Wang, X., Zhang, S., Zhang, H., Gu, Z., et al. (2025a). Acoustic monitoring and structural damage evaluation of tensile fracture in various materials using optical fiber sensing. *Physics of Fluids.* 37, 027184. doi:10.1063/5.0256902

Zhou, X., Liu, X. F., Zhao, X. H., Wang, X. R., Liu, C., and Zhang, S. Q. (2025b). Brazilian splitting crack propagation characteristics and micro-mechanism in center cracked circular discs of coal specimen. *Theoretical and Applied Fracture Mechanics* 141, 105327. doi:10.1016/j.tafmec.2025.105327

Zhou, X., Liu, X. F., Wang, X. R., Liu, Y. B., Xie, H., and Du, P. F. (2023). Acoustic emission characteristics of coal failure under triaxial loading and unloading disturbance. *Rock Mech. Rock Eng.* 56, 1043–1061. doi:10.1007/s00603-022-03104-2

Zhou, X., Liu, X. F., Wang, X. R., Gu, Z. J., Xie, H., and Zhang, S. Q. (2024). Mechanical and fracture characteristics in center cracked circular discs of coal specimens with different sizes: an experimental investigation. *Theor. Appl. Fract. Mech.* 129, 104245. doi:10.1016/j.tafmec.2023.104245

Zhuo, Y. Q., Guo, Y. S., Ji, Y. T., and Ma, J. (2013). Slip synergism of planar strike-slip fault during meta-instable state: experimental research based on digital image correlation analysis. *Sci. China-earth Sci.* 56, 1881–1887. doi:10.1007/s11430-013-4623-4